

Observations of the *Hubble Deep Field South* with the *Infrared Space Observatory* - I. Observations, data reduction and mid-infrared source counts

Seb Oliver^{1,2}, Robert G. Mann^{1,3}, Ruth Carballo^{4,5}, Alberto Franceschini⁶, Michael Rowan–Robinson¹, Maria Kontizas⁷, Anastasios Dapergolas⁸, Evangelos Kontizas⁸, Aprajita Verma¹, David Elbaz⁹, Gian Luigi Granato⁶, Laura Silva¹⁰, Dimitra Rigopoulou¹¹, J. Ignacio Gonzalez–Serrano⁵, Steve Serjeant^{1,12}, Andreas Efstathiou¹, Paul P. van der Werf¹³

¹ *Astrophysics Group, Imperial College London, Blackett Laboratory, Prince Consort Road, London SW7 2BZ*

² *Astronomy Centre, School of Chemistry, Physics and Environmental Science, University of Sussex, Falmer, Brighton, BN1 9QJ*

³ *Institute for Astronomy, University of Edinburgh, Royal Observatory, Blackford Hill, Edinburgh, EH9 3NJ*

⁴ *Departamento de Matematica Aplicada y CC, Universidad de Cantabria, Avda. Los Castros s/n, 39005 Santander, Spain*

⁵ *Instituto de Física de Cantabria (CSIC-UC), Avda. Los Castros s/n, 39005 Santander, Spain.*

⁶ *Dipartimento di Astronomia — Università di Padova, Vicolo dell'Osservatorio 5, I-35122, Padova, Italy*

⁷ *Department of Physics, University of Athens, Panepistimiopolis, GR-15783, Zografos, Greece*

⁸ *Astronomical Institute, National Observatory of Athens, Lofos Nymfon, Thission, P.O. Box 20048, 11810 Athens, Greece*

⁹ *DSM/DAPNIA/Sap, CE - Saclay, Orme des Merisiers - Bat 709, 91191 Gif-sur-Yvette Cedex, France*

¹⁰ *Astrophysics Sector, SISSA, Via Beirut 2-4, 34013 Trieste, Italy*

¹¹ *Max-Planck-Institut für extraterrestrische Physik, Postfach 1603,85740 Garching, Germany*

¹² *Unit for Space Sciences and Astrophysics, School of Physical Sciences, University of Kent, Canterbury, Kent, CT2 7NZ*

¹³ *Leiden Observatory, P.O. Box 9513, NL-2300 RA Leiden, The Netherlands*

28 October 2018

ABSTRACT

We present results from a deep mid-infrared survey of the Hubble Deep Field South (HDF–S) region performed at 7 and 15 μ m with the CAM instrument on board the *Infrared Space Observatory* (ISO). The final map in each band was constructed by the coaddition of four independent rasters, registered using bright sources securely detected in all rasters, with the absolute astrometry being defined by a radio source detected at both 7 and 15 μ m. We sought detections of bright sources in a circular region of radius 2.5 arcmin at the centre of each map, in a manner that simulations indicated would produce highly reliable and complete source catalogues using simple selection criteria. Merging source lists in the two bands yielded a catalogue of 35 distinct sources, which we calibrated photometrically using photospheric models of late-type stars detected in our data. We present extragalactic source count results in both bands, and discuss the constraints they impose on models of galaxy evolution models, given the volume of space sampled by this galaxy population.

Key words: galaxies: formation - infrared: galaxies - surveys - galaxies: evolution - galaxies: star-burst - galaxies: Seyfert

1 INTRODUCTION

One of the most notable achievements of the *Hubble Space Telescope* (HST) has been to lead and inspire

Table 1. *ISO* Observation Log. This table gives some details from the *ISO* databases for each of the *ISO* HDF-S observations: The target name, coordinates, Observation Number (OSN), the time spent on target in seconds (TDT), the revolution number (REV), the status and the date. Note that two observations (OSN 4 and 8) failed, but were repeated on 27 and 29 November.

TARGET	RA (J2000)	DEC (J2000)	OSN	TDT	REV	STATUS	Date
HDF-1 LW2	22h 32m 57.5s	-60d 33' 10.0"	1	7825	702	Observed	17 Oct 1997
HDF-4 LW2	22h 32m 53.9s	-60d 33' 00.0"	7	7825	702	Observed	17 Oct 1997
HDF-2 LW2	22h 32m 56.4s	-60d 32' 51.8"	3	7825	704	Observed	19 Oct 1997
HDF-4 LW3	22h 32m 53.9s	-60d 33' 00.0"	8	7497	722	Failed	6 Nov 1997
HDF-2 LW3	22h 32m 56.4s	-60d 32' 51.8"	4	7497	722	Failed	6 Nov 1997
HDF-3 LW2	22h 32m 55.0s	-60d 33' 18.2"	5	7825	723	Observed	7 Nov 1997
HDF-3 LW3	22h 32m 55.0s	-60d 33' 18.2"	6	7497	723	Observed	7 Nov 1997
HDF-1 LW3	22h 32m 57.5s	-60d 33' 10.0"	2	7497	723	Observed	8 Nov 1997
HDF-4 LW3	22h 32m 53.9s	-60d 33' 00.0"	8	7497	742	Observed	27 Nov 1997
HDF-2 LW3	22h 32m 56.4s	-60d 32' 51.8"	4	7497	745	Observed	29 Nov 1997

the concerted multi-wavelength programme of observations of the *Hubble Deep Field* (HDF, Williams et al. 1996) region. As part of that campaign we observed the HDF at 6.7 and 15 μm using the *ISO*-CAM instrument (Cesarsky et al. 1996) on the *Infrared Space Observatory* (*ISO*; Kessler et al. 1996). From the maps that resulted from these observations (Serjeant et al. 1997) we extracted sources in both bands (Goldschmidt et al. 1997), whose number counts implied a strongly-evolving population of starburst galaxies (Oliver et al. 1997). Following the association of these sources with galaxies in optical HDF catalogues (Mann et al. 1997) we derived an infrared luminosity density that suggested a higher star-formation rate in the HDF region than indicated by optical studies (Rowan-Robinson et al. 1997): the importance of dust obscuration in estimating the star-formation rate has been confirmed by other *ISO* surveys e.g. (Flores et al. 1999), from detailed consideration of the optical measures of star formation (Steidel et al. 1999) and from the intercomparison of different star formation indices (Cram et al. 1998).

Difficulties with the *ISO* 6.7 μm data led us to re-observe the HDF at that wavelength. These new data, together with a consensus view of the interpretation of our *ISO* HDF-N data derived from the combined experience of the several groups that re-analyzed them (Aussel et al. 1999, Desert et al. 1999) in the light of developing knowledge of the properties *ISO*-CAM data will be the topic a subsequent paper, as will a revised and updated scientific interpretation of the *ISO* HDF data.

Following the success of the HDF project, a similar programme of *HST* observations was planned for the southern hemisphere, and the region of the Hubble Deep Field South (HDF-S) has become the target of a similarly wide-ranging multi-wavelength programme* of observations. This paper describes our

contribution to that project, through our mapping of the HDF-S with *ISO*-CAM. We mapped the HDF-S WFPC2 fields at both 6.7 and 15 μm , as in the northern HDF, but with a slightly different observational strategy (described in Section 2), motivated by our experience with the *ISO* HDF data. Section 3 describes our data reduction procedures, and Sections 4 and 5 source extraction and photometric calibration, respectively. In Section 6 we describe simulations of the data performed to facilitate assessment of the reliability of the source catalogues we present in Section 7 and to compute the effective area of the survey as a function of flux cut, as this is required for computation of the source counts, which is the topic of Section 8. Finally, Section 9 presents a discussion of the results of this paper and the conclusions we draw from them. In an accompanying paper (Mann et al., 2002, hereafter Paper II) we seek associations for these sources in optical/near-infrared and radio surveys of the HDF-S region, and present star formation rate estimates for the sources for which we find associations.

2 THE OBSERVATIONS

The team undertaking the European Large Area *ISO* Survey (ELAIS[†], Oliver et al. 2000) were awarded 61.3 ks to observe the HDF-S in a successful application to the *ISO Supplemental Call*. The observations were carried out using the *ISO*-CAM instrument (Cesarsky et al. 1996) between 17 October and 29 November 1997. In the light of an increased understanding of the properties of *ISO*-CAM data, and of the galaxy population they probe, gained by our own *ISO* HDF observations and from other deep *ISO*-CAM surveys (e.g. Taniguchi et al. 1997, Elbaz et al. 1999) we made some alterations to the observing strategy that we

* Details of the HDF-S programme can be found at <http://www.stsci.edu/ftp/science/hdf/hdfsouth/hdfs.html>

[†] For details see the ELAIS Home Page: <http://astro.ic.ac.uk/elais>

Table 2. Observation parameters for the ISO HDF South

Parameter	OSN	
	1,3,5,7	2,4,6,8
Filter	LW2	LW3
Band centre [μm]	6.7	15
Gain	2	2
Tint [s]	10	5
NEXP	10	20
NSTAB	80	80
PFOV [arcsec]	6	6
M, N	8,8	8,8
dM, dN [arcsec]	27	27

used for the *ISO* HDF, as reported by Serjeant et al. (1997).

As listed in Table 1, eight rasters were taken, one with the LW2 ($6.7 \mu\text{m}$) and one with the LW3 ($15 \mu\text{m}$) filter at each of four positions, with raster centres offset by fractional pixel widths to improve the spatial resolution of the final map obtained by their coaddition. The parameters used for these observations are listed in Table 2. The values for *Gain*, *Tint* (the integration time per readout), *NEXP* (the number of readouts per pointing), and *NSTAB* (the number of readouts allowed for stabilization prior to the raster) remained unchanged, as those used by Serjeant et al. (1997) still appeared to be optimal for the required depth. The pixel field of view, *PFOV*, at $6.7 \mu\text{m}$ was changed from $3''$ to $6''$ (matching that used at $15 \mu\text{m}$), since the *ISO*-HDF images at $6.7 \mu\text{m}$ were not confusion limited, and the improvement in signal-to-noise ratio, and areal coverage, obtained by moving to larger pixels was expected to outweigh the loss in resolution. The other significant change was to increase the raster step size, which had two effects. Firstly, with the step size now larger than the point spread function (PSF), consecutive pointings would no longer have significantly correlated signal, making the removal of noise which was correlated in time (e.g. $1/f$ noise) much easier. Secondly, the larger pixel area meant that the full survey area could be covered by each individual 8×8 raster, with the complete survey being made up by stacking the four independent rasters in each passband. This contrasts with the technique adopted in the *ISO*-HDF of partially overlapping deeper rasters, and has several advantages: it reduces correlated noise problems; readily provides direct assessment of source reliability, through looking for detections in the independent maps; and facilitates the registration of the maps, through the presence of a greater number of bright sources in each raster (helped further by the lower Galactic latitude of the HDF-S, providing more bright stellar sources). In Figure 1 we show the location of our ISO rasters with respect to those of various optical/near-IR datasets taken in the HDF-S area: this illustrates that while none of these surveys covers the whole of the area we mapped with ISO, the region from which we se-

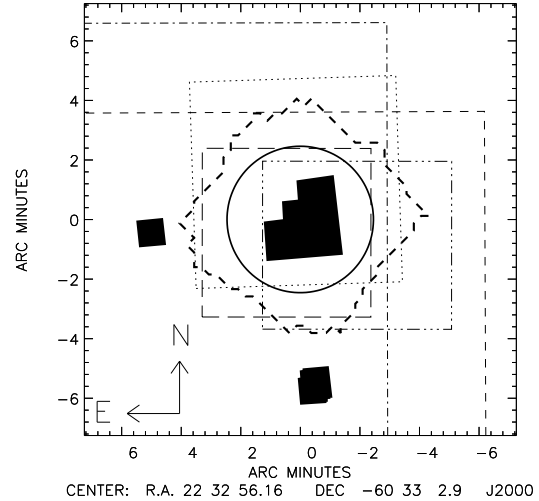


Figure 1. This figure shows the location of our ISO rasters with respect to those of other datasets taken in the area. The shaded regions mark the *HST* fields, with the STIS and NICMOS fields to the east and south of the WFPC2 field, respectively. The thick-dashed irregular shape and the solid circle show, respectively, the maximum extent of our ISO coverage (the coverage in the two bands differs slightly) and the region from which the source catalogues of Section 7 were selected. The remaining lines show boundaries of four optical/near-IR surveys discussed in Paper II, as follows: (i) dotted line – AAT prime focus imaging survey of Verma et al. (2002); (ii) dashed line – CTIO BTC survey of Gardner et al. (1999); (iii) dot-dashed line – CTIO BTC survey of (Walker 1999); (iv) dot-dot-dot-dashed line – ESO EIS optical imaging survey of da Costa et al. (1998); and (v) long dashed line – ESO EIS near-infrared survey of da Costa et al. (1998).

lect sources in Section 7 is covered, at least partially, by several imaging surveys in different wavebands, as discussed in more detail in Paper II.

3 DATA REDUCTION

Similarly to the *ISO* HDF data, and in contrast to the ELAIS data (Oliver et al. 2000), we do not expect to detect many sources in the signal from a single pixel as it scans across the sky (the “time-line”). Most sources will only be detected when all the overlapping scans are co-added. The data reduction thus proceeds by filtering each time-line for artifacts and then combining these to produce a map for each raster. These raster maps are then co-aligned and co-added to produce a single map from which sources can be extracted. Most of the data reduction described in these sections was carried out using the Interactive Data Language (IDL

[‡]), with some steps done using the *ISO*-CAM Interactive Analysis (CIA: Ott et al. 1998) software.

3.1 Time-series Filtering

The first stage in the data reduction treats the scan of each pixel across the sky independently. This time-series is filtered to reduce the impact of noise features and optimize the signal at each static pointing. At this stage the individual pixel responses are also estimated using a Gaussian fit to the scan to determine a sky flat-field correction which is normalized to the median from the central pixels, as in Serjeant et al. (1997).

The original data reduction of the *ISO*-HDF applied a simple threshold filtering of very short time-scale features (cosmic ray hits), and we apply the same method to these data. However, for the original reduction of the *ISO*-HDF data we anticipated that there might be significant source confusion, leading to real structure in the sky background, and so we did not apply any filtering for low frequency noise. At $6.7\ \mu\text{m}$ the *ISO*-HDF was not significantly confused and the revised observing strategy we used for the HDF-S reduces any correlated signal between successive pointings. We thus decided to adopt a more aggressive filtering strategy for these data. It can be seen from Figure 2 that there is significant correlated noise at a variety of time-scales. The filtering technique we adopt is similar to that used by Desert et al. (1999). We subtract a time variable background level from all the readouts in a time-line. The background level is estimated for each pointing, being the average of the readouts in the two previous and the two subsequent pointings.

This filtering scheme will go awry where sources lie in the pixels used for background estimation, so we perform a second iteration. We mask out the bright sources detected from the first pass (see Section 4) and then an additional filter is applied to exclude readouts not already flagged as sources that deviate from the estimated background by more than 5σ . This procedure will not affect remaining sources which would be at a very low level of significance in single pointings. After applying these filters the mean of the readouts is calculated over each pointing, and the resulting noise statistics are summarized in Table 3.

3.2 Mosaicing Independent Rasters

The detector image at each raster position needs to be projected onto the sky. For this process we use a “shift-and-add” technique. We generate a blank sky map with $1''$ pixels. Then, for each raster pointing we determine which sky pixels lie within the geometrical footprint of each detector pixel. In doing this we

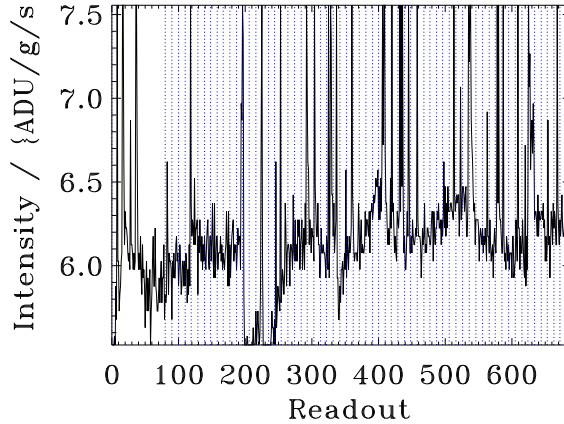


Figure 2. Example pixel history. Minimum and maximum levels are adjusted to exclude extreme outliers. The positions of slews are marked with vertical dotted lines. This particular pixel is row 16, column 16 from the $6.7\ \mu\text{m}$ observation HDF-1

take into account the field distortions (Aussel et al. 1999) in the *ISO*-CAM data: *N.B.* it was not possible to take these into account in our original *ISO*-HDF-N reductions since the distortions had not been well characterized at that time. The average intensity of all detectors covering a sky pixel is calculated using a number of estimators. It was found that the median produced the smallest fluctuations in the resulting sky maps (suggesting that some residual non-Gaussian noise was present), and so we adopted this estimator. The use of the geometrical footprint was a somewhat arbitrary choice and not the optimal one for point sources; since in the extraction of point sources we convolve the image with another kernel we have broadened the effective point spread function by using this.

The noise in these maps is estimated by constructing a histogram of pixel values and fitting this with a Gaussian, as well as computing directly an RMS. However, since the number of independent pointings varies as a function of sky position, we calculate these statistics for regions with similar numbers of pointings. The results from these assessments indicate that noise reduces as expected for independent pointings (i.e. the residual noise-correlations between pixels are at a very low level: see Figs. 3 and 4). The RMS fluctuations in the maps are larger than the σ estimated from the Gaussian fitting, indicating non-Gaussian fluctuations, which we attribute to real sources, either distinct or confused.

The noise can also be investigated by corrupting the astrometry information and thereby diluting the signal from real sources. We describe this “mis-mosaicing” technique in more detail in Section 6. The noise statistics from a typical mis-mosaiced field, together with those from the final images, are also summarized in Table 3. The σ values from the

[‡] see www.rsinc.com

Table 3. Statistical properties of the reduced data sets. All units are instrumental (ADU/g/s/pixel). The mode is taken from all valid readouts and pixels. Fluctuations are estimated by fitting a Gaussian to the distribution (first lines) and by calculating the RMS (second lines). The difference between these two measures gives some idea of the non-Gaussianity. Fluctuations are quoted for the readout and pointing time scales (third and fourth column) and are estimated from the time line of one pixel near the centre of the image. In the filtered readouts the RMS fluctuations are similar to the σ estimated from a Gaussian fitting, suggesting that the noise is reasonably Gaussian. If the fluctuations are white noise they should reduce by a factor of \sqrt{NEXP} (i.e. $\sqrt{10}$ at $6.7 \mu\text{m}$ and $\sqrt{20}$ at $15 \mu\text{m}$) when averaging over a pointing. The fluctuations over an entire detector image (after coaddition of all readouts in a pointing) are quoted in column 5 and estimated from all valid pixels and images. The noise in the images is calculated separately for regions with different numbers of pointings and is fitted as \sqrt{NPOINT} , the values quoted in the Table are for $NPOINT = 1$, and for our maps $\overline{NPOINT} \sim 13$. Finally, we compute the noise statistics for one of our mis-mosaiced maps (as described in Section 6), column 6. Here we only quote the σ values as the RMS measures are more strongly influenced by the residual source signals in parts of the images with small values of $NPOINT$.

Observation	Mode	Readout		Point.	Image	Mis-mosaiced
		Raw	Filt.			
HDF-1 LW2	6.30	0.21	0.14	0.08	0.089	0.088
		2.98	0.14	0.03	0.22	
HDF-2 LW2	6.47	0.13	0.11	0.06	0.081	0.079
		1.90	0.11	0.01	0.25	
HDF-3 LW2	7.38	0.43	0.19	0.19	0.11	0.10
		3.88	0.21	0.07	0.20	
HDF-4 LW2	6.37	0.20	0.13	0.08	0.083	0.083
		2.32	0.14	0.04	0.22	
HDF-1 LW3	33.49		0.33	0.13	0.22	0.25
			0.32	0.06	0.29	
HDF-2 LW3	37.39		0.30	0.12	0.24	0.26
			0.29	0.05	0.30	
HDF-3 LW3	34.04		0.34	0.18	0.23	0.25
			0.34	0.14	0.30	
HDF-4 LW3	35.09		1.53	1.50	1.28	1.28
			1.23	2.80	1.50	

mis-mosaiced fields are very similar to the real fields confirming that these are reasonably representative of the noise. The RMS values for the mis-mosaiced fields were invariably higher but this was because the RMS in regions of lower coverage were higher, since real sources could not be properly filtered out in these regions: this is consistent with our hypothesis that much of any residual non-Gaussian noise is due to real sources.

3.3 Raster registration

Since the survey strategy means that each independent raster covers approximately the same relatively large area (c.f. *ISO*-HDF) a number of bright sources are clearly visible in each raster. For each band we thus selected a number of these sources which had good signal-to-noise and which were not located close to the edges of the map (where the noise is less well behaved and the field distortions are more significant) for use in registering the four maps. The positions of these sources are denoted by $(x_{i,j}, y_{i,j})$, where the i subscript labels the source and j subscript labels the map. We then computed the mean (\bar{x}_i, \bar{y}_i) position of each source across all four independent maps, weighted by w_j , the mean SNR of that map (estimated from the mean SNR in all the

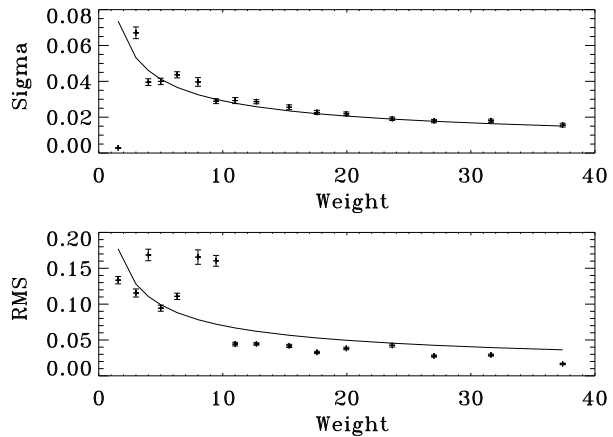


Figure 3. Noise estimates as a function of number of pointings ($NPOINT$, labeled as “Weight”), for the LW2 ($6.7\mu\text{m}$) HDF-1 observations. Upper panel σ from a Gaussian fit, lower panel RMS . All units are ADU/g/s/pixel

sources). For each map we then estimated a mean offset $\delta x_j = \sum w_i(x - \bar{x}_i) / \sum w_i$, where the weight for each source w_i is estimated from the mean SNR for that source over all maps. This process does not require any assumptions about the relationship between the *ISO* sources and sources detected in any

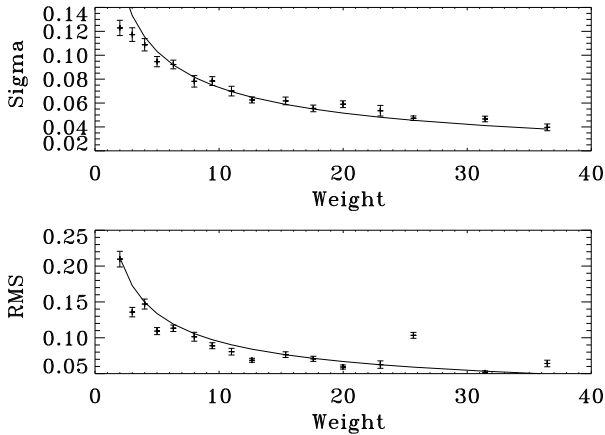


Figure 4. Noise estimates as a function of number of pointings (*NPOINT*, labeled as “Weight”) for the LW3 ($15\mu\text{m}$) HDF-1 observations. Upper panel σ from a Gaussian fit, lower panel *RMS*. All units are ADU/g/s/pixel

other wavebands, and is also likely to be more robust than the cross-correlation of the full image (including the noisy regions) with, for example, a radio map of the same field. The mean offsets were rounded to the nearest pixel ($1''$). The overall astrometric reference frame was defined later, see Section 7 below.

The registered images were then co-added using an inverse variance weighting. The variance estimated was proportional to the number of pointings within a raster and scaled using the value for σ/\sqrt{NPOINT} estimated from the Gaussian fitting described above. The resulting maps had some small residual background. This background (which was not always positive) should in principle have been removed by the time-line filtering, although some residual would be expected from an overall gradient in the time-lines. In any case, the background was estimated from the mean of the Gaussian fitted to the histogram of the map pixel values, which was a good estimate of the mode. The resulting co-added signal-to-noise maps at 6.7 and $15\mu\text{m}$ are presented in Figures 5 and 6, respectively.

4 SOURCE DETECTION

We expect most of the sources in these maps to be point sources, so it is more appropriate to detect sources by a convolution technique rather than to use a connected pixel algorithm. We also expect to be close to the confusion limit, so the choice of smoothing kernel is important: where the signal is dominated by a single source the optimal kernel is the point-spread function (PSF), while, for confused images, the likely presence of other sources in the wings of the PSF will make this kernel non-optimal. The solution is either to truncate the PSF kernel at some appropriate distance or to use a narrower kernel. Theoretically, the PSF

should be that of the Airy disk defined by the telescope aperture, convolved with the square pixel aperture of $6''$, and the *CIA* calibration PSFs are similar to this. In practice, however, the PSF will be broadened by our mapping footprint, and any inaccuracies in registration and/or the field-distortion correction applied. The profiles we used for source extraction are Gaussian, with a FWHM of $6''$ and $10''$ at $6.7\mu\text{m}$ and $15\mu\text{m}$ respectively, and both are truncated at a radius of $12''$. Table 4 compares the FWHM values for these model PSFs with those estimated from the sources detected in the data. It shows that, as desired, the model PSFs used for source detection, while being slightly larger than the theoretical PSF, are slightly narrower than the empirical PSF derived from the sources themselves.

An initial candidate list of sources was selected in each band, comprising peaks in the respective convolved, co-added signal-to-noise (*SNR0*) map above 3σ . For each of these peaks we returned to the individual raster maps and computed a number of additional statistics. These included the signal-to-noise ratio in each map (*SNRn*, $n = 1 - 4$) and the number of pointings at the source position in these maps (*NPOINTn*, $n = 1 - 4$). One quantity derived (*PICK*) was the number of detections with *SNRn* > 1 and *NPOINTn* > 4 . We also computed the mean and RMS deviation of the flux for the source over all maps, together with the ratio of these (*SNR5*). Using the simulations described in Section 6 we could then assess and employ these various statistics to define suitable simple criteria for filtering the candidate list to produce a highly reliable source list with reasonable completeness.

5 PHOTOMETRIC CALIBRATION

One difference between the HDF South and the HDF North is that the former is located at lower Galactic latitude and so has a higher proportion of stars. This is extremely useful for the calibration of the *ISO* data, since a number of the bright stars are detected, and photospheric model spectra can be used to estimate their 6.7 and $15\mu\text{m}$ fluxes. Our calibration procedure was to identify a number of stars for which we could accurately predict mid-infrared fluxes and then measure their fluxes directly from the *ISO* maps. Since the stars are known sources with known positions we are not concerned about the reliability of their detection, so these stars do not necessarily appear in our source lists, and their fluxes can be fainter than the faintest sources in our complete samples.

To model accurately the stellar fluxes we ideally need spectral classifications and accurate magnitudes for the stars. We inspected and classified the star spectra taken on the AAT with the LDSS (Glazebrook *et al.*, in preparation: see <http://www.aao.gov.au/hdfs/Redshifts/>). We

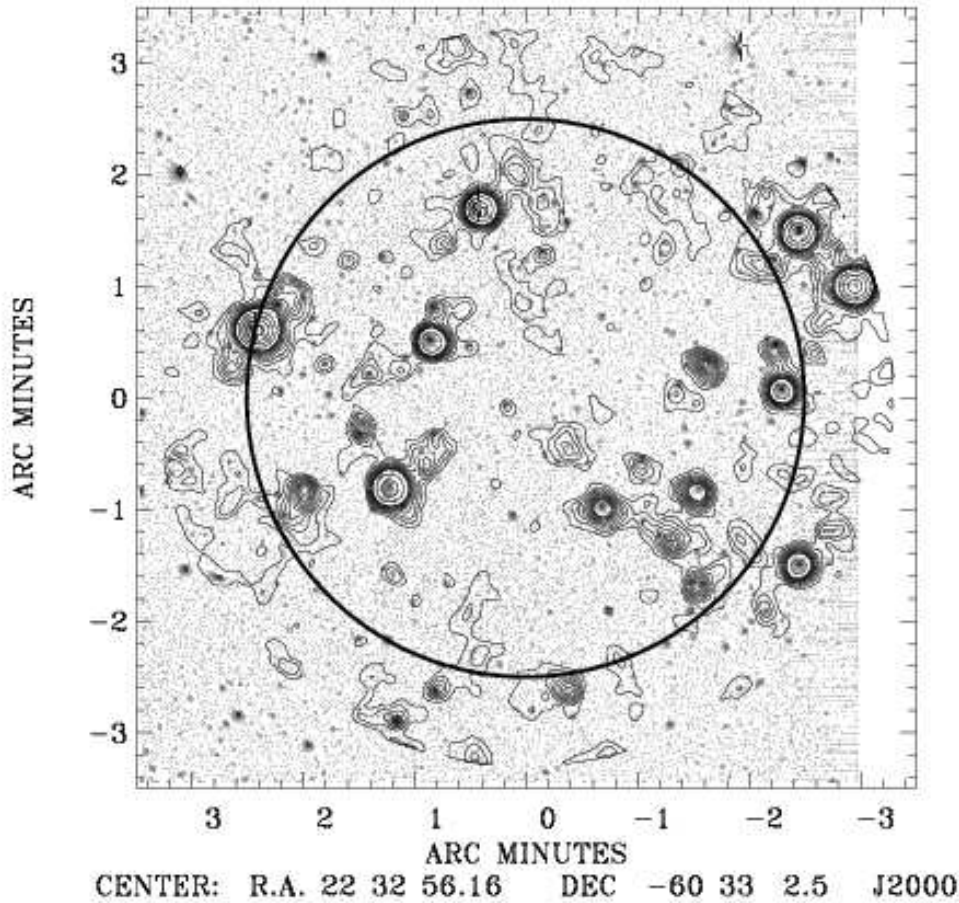


Figure 5. LW2 ($6.7\mu\text{m}$) signal-to-noise map. This figure plots contours in the LW2 signal-to-noise map after it has been smoothed with the point-source-detection kernel. The lowest contour level has signal-to-noise = 1 and subsequent intervals are 1 until signal-to-noise = 10 where after the contours are logarithmically spaced. *ISO* data is plotted out to a radius of $3.3'$. The background image is the CTIO BTC survey of (Walker 1999). The circle indicates the $2.5'$ boundary of the region within which we extracted sources for our catalogues. Overlays of subsections of the data onto colour HST images are available from our WWW page (astro.ic.ac.uk/hdfs).

Table 4. Full-width-half-maxima (FWHM, in arcsec) for theoretical and empirical point-spread functions: see text for details. The column marked “used” gives the FWHM values for the model PSFs used for source extraction, the “star” PSF is estimated from the brightest star in the LW2 image, and the “sources” PSF from the sources detected above 20σ in each image (8 sources for LW2 and 1 source for LW3). Empirical FWHM are calculated by fitting a 2-D Gaussian to the observed PSF.

Filter	$\lambda[\mu\text{m}]$	Airy disk + pixel	CIA	Used	Star	Sources
LW2	6.7	5.8	7.3	6.0	10.4	8.3
LW3	15	7.3	9.0	10.0		10.4

supplemented this list with additional stars that had been detected in our *ISO* maps (prior to the filtering applied to produce a highly reliable source list presented in Section 7). We cross-correlated all these objects with the ESO optical catalogues (da Costa et al. 1998) and the AAT catalogues (Verma et al. 2002) to obtain optical and NIR magnitudes. This combined sample of stars is listed in Table 5.

For each star we returned to the *ISO* maps and extracted the flux and uncertainty in the flux, exactly as we did for our *ISO* detected source list. For a number of them which had good *ISO* detections at $6.7\mu\text{m}$ and good optical information we estimated the expected $6.7\mu\text{m}$ and $15\mu\text{m}$ fluxes using the models

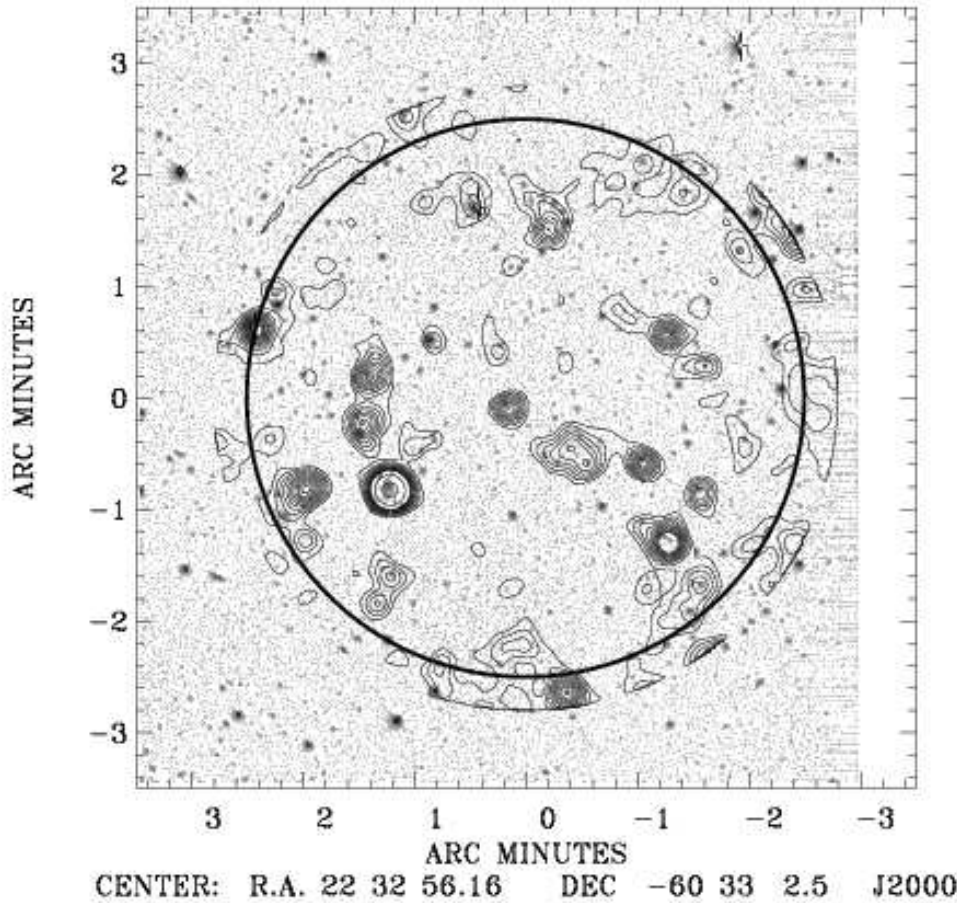


Figure 6. LW3 ($15\mu\text{m}$) signal-to-noise map. This figure plots contours in the LW3 signal-to-noise map after it has been smoothed with the point-source-detection kernel. The lowest contour level has signal-to-noise = 1 and subsequent intervals are 1 until signal-to-noise = 10 where after the contours are logarithmically spaced. *ISO* data is plotted out to a radius of $2.8'$. The background image is the CTIO BTC survey of (Walker 1999). The circle indicates the $2.5'$ boundary of the region within which we extracted sources for our catalogues. Overlays of subsections of the data onto colour HST images are available from our WWW page (astro.ic.ac.uk/hdfs).

of Kurucz[§]. Where a spectral classification was not available, the temperature was estimated from the optical photometry alone. The predicted fluxes are plotted against the observed fluxes for the two wavebands in Figures 7 & 8. We performed a linear fit to these data constrained to pass through the origin. For the $6.7\mu\text{m}$ data we excluded the star at 22 32 36.23 - 60 31 31.5, which was a significant outlier and had neither a spectral type, nor NIR magnitudes. For the $15\mu\text{m}$ data we excluded 22 32 36.23 - 60 31 31.5, as we had at $6.7\mu\text{m}$, and also 22 32 36.19 - 60 34 31.5, which was an outlier in both fits and also had neither NIR nor classification information. The fits are remarkably good once the few outliers have been excluded, and provide us with a good flux calibration, which is used

throughout this paper. From the scatter in the correlation the errors in this calibration are estimated to be 36 per cent at $6.7\mu\text{m}$ and 28 per cent at $15\mu\text{m}$.

6 SIMULATIONS

The noise properties of the *ISO* data are sufficiently complicated that simulations are essential in order to determine accurately the quality of the information extracted from our maps. In particular we wish to assess the reliability of the source catalogues presented in Section 7 and to calculate the effective area over which we could have detected sources above a given flux limit, to facilitate computation of source counts in Section 8. We have thus constructed a number of simulated datasets which mimic the noise properties of the real data as faithfully as possible.

[§] see kurucz.harvard.edu/

Table 5. Stars in HDF South. This is an inhomogeneous list of stars collected for the process of calibration. Spectral types were determined from the AAT spectra. Optical magnitudes are in the AB system and come from the ESO survey (da Costa et al. 1998) or the AAT survey (Verma et al. 2000). Observed 6.7 and 15 μ m fluxes (S_o) are in raw instrumental units. Fluxes are taken directly from the maps. One flux was measured to be negative (with large error) and is quoted as such, since this would be valid in a calibration fit, however this point has not been used in the calibration. Predicted 6.7 and 15 μ m (S_p/μ Jy) are estimated for a few of these objects as described in the text. Magnitudes quoted as 99.99 indicated saturated measurements

RA,Dec (J2000)	Type	U	B	V	R	I	J	H	K	$S_{o6.7}$	S_{o15}	$S_{p6.7}$	S_{p15}
22 32 31.94 -60 32 00.7			11.94		12.17					77.42	23.79		
22 32 36.19 -60 34 31.5		21.56	19.81	18.14	17.00	15.80				17.66	10.79	626.0	134.0
22 32 36.23 -60 31 31.5		20.38	18.51	16.92	15.80	14.60				42.17	26.01	600.0	130.0
22 32 37.48 -60 32 57.3		21.30	19.38	17.73	16.70	15.70				12.56	6.33	611.0	134.0
22 32 39.41 -60 31 22.6	G0 V	18.02	17.03	16.38	16.10	16.00				2.17	7.23		
22 32 39.88 -60 33 23.6	M2.5 V	99.99	99.99	99.99	99.99	26.40				0.40	5.38		
22 32 40.70 -60 33 24.1										0.39	5.30		
22 32 43.51 -60 33 51.0		20.51	20.11	20.23	20.01	19.85	19.78	19.42	19.53	4.35	10.76		
22 32 47.45 -60 32 00.0	M2.5 V	99.99	24.05	22.59	21.31	19.80	18.36	18.22	18.42	0.45	-1.17		
22 32 50.50 -60 34 00.8	M2 V	21.98	20.24	18.71	17.90	17.13	16.41	16.21	16.49	3.74	0.96		
22 32 50.62 -60 34 04.0		21.90	20.23	18.70	17.84	17.01	16.42	16.21	16.49	3.74	1.30	166.0	36.5
22 32 54.90 -60 31 44.1		23.41	21.70	20.18	19.30	18.32	17.51	17.26	17.51	0.92	6.34		
22 32 56.72 -60 35 49.5		27.63	25.81	24.35	23.50	22.90				1.00	9.69		
22 32 59.50 -60 31 19.2	G2 III	15.11	14.63	13.91	14.14	13.60	13.57	13.61	14.03	20.82	6.43	1096.0	230.0
22 33 02.70 -60 35 39.5		20.79	18.98	17.77	17.22	16.80	16.67	16.51	16.86	2.33	7.42		
22 33 02.76 -60 32 13.3	M3 V	23.00	21.26	19.76	18.87	17.74	16.90	16.76	17.01	1.38	0.70	105.0	23.0
22 33 03.07 -60 32 30.8	M1 V	20.01	18.15	16.83	16.20	15.53	14.97	14.73	15.04	9.29	4.28	550.0	118.0
22 33 08.20 -60 33 21.2	K4 V				17.30		16.75	16.57	16.97	1.91	12.14		
22 33 12.09 -60 34 16.7							22.46	21.76	21.10	1.39	8.16		
22 33 15.83 -60 32 24.0	M2 V		15.80		13.95	13.11	12.47	12.24	12.53	90.78	31.03	6000.0	1311.0
22 33 19.00 -60 32 27.8	M2 V				20.83					1.53	6.40		
22 33 20.83 -60 34 35.1	G1 V				17.10						6.74		
22 33 24.02 -60 33 10.6	G3.5 V				17.91					0.78			
22 33 24.22 -60 33 52.9	M3 V				16.32					16.07	15.89		
22 33 26.22 -60 32 05.9	F8 III				15.93								
22 33 28.05 -60 33 38.0	G5 V				19.96								
22 33 28.93 -60 35 01.5	M2.5 V				21.53								
22 33 31.23 -60 33 43.9	M3 V				19.48								
22 33 31.67 -60 33 41.9	M2 V				24.04								
22 33 37.40 -60 34 03.2	M3 V				18.84								
22 33 46.17 -60 34 03.4	M2 III				19.95								

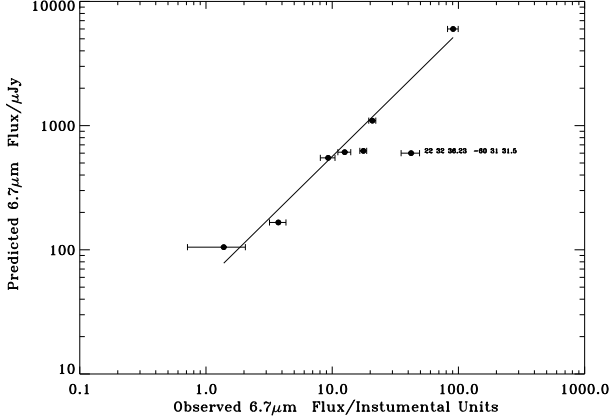


Figure 7. Calibration of the 6.7 μ m data. The linear fit is constrained to pass through the origin and excludes source 22 32 36.23 -60 31 31.5. The fit is S_p/μ Jy = $56 \pm 20 S_o/\text{Instrumental Unit}$.

6.1 Method

As discussed earlier, most sources will not be detected significantly in individual time-lines, only appearing after co-addition of many observations of the same patch of sky. By corrupting the astrometric information before constructing the maps it is thus possible to remove most of the real source signal, the remaining fluctuations being almost entirely due to noise. This technique was employed in our reduction of the HDF North data, where we corrupted the astrometric information by randomizing the apparent location of

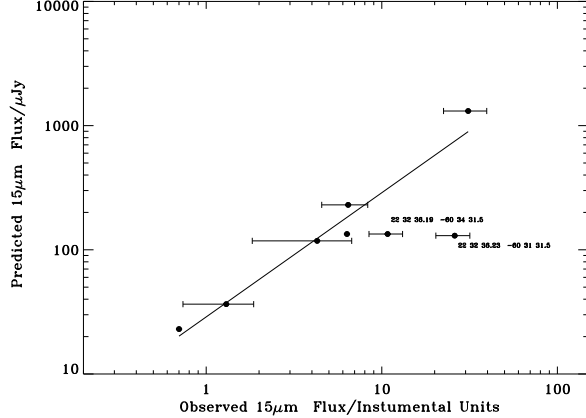


Figure 8. Calibration of the 15 μ m data. The linear fit is constrained to pass through the origin and excludes sources 22 32 36.19 -60 34 31.5 and 22 32 36.23 -60 31 31.5. The fit is S_p/μ Jy = $29 \pm 8 S_o/\text{Instrumental Unit}$.

each pixel within the detector array for each pointing position. This technique was not entirely satisfactory, since noise that was correlated between neighbouring pointings and pixels was also artificially reduced in the resulting maps. A much better technique is to corrupt the astrometric information coherently for the whole detector, so that real sources are still dispersed, while maintaining the time-ordering of the data, and the localization of pixel groups. This technique should account for all sources of instrumental noise. There are seven possible ways of achieving this for a given

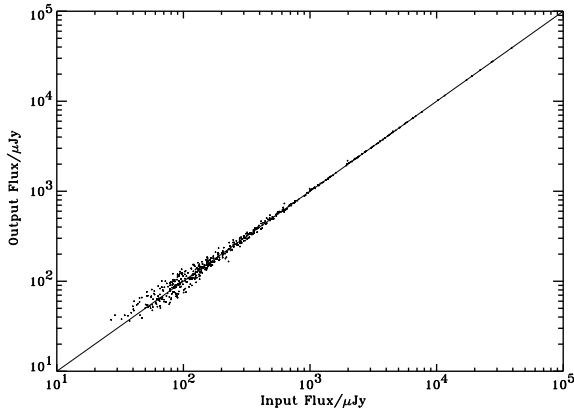


Figure 9. Output flux vs Input flux from the simulated data at $6.7\mu\text{m}$.

raster, corresponding to each independent reflection and rotation of the detector through 90 degrees. Real sources that happen to lie near the axis of symmetry in some pointings will be less corrupted than others, so we expect the resulting “noise” maps to have some fluctuations due to real sources and they are thus pessimistic estimates of the noise. For each observation we generated all seven possible “noise” maps. Since the HDF South field is observed four times with each band there are thus $7^4 \equiv 2401$ different combinations of “noise” maps that we can use to simulate a completed map.

One source of noise that is not included in these “noise” maps is confusion noise due to real sources. To account for this we generated artificial source lists generated from a number count distribution which was a reasonable fit to a preliminary analysis of the total source counts (i.e. including both stars and galaxies). We generated 25 independent synthetic source lists and added each of these sources list to a randomly selected set of “noise” maps, using the empirical point spread function discussed in Section 4. The sources were placed on the maps at their nominal positions, thus we did not include any additional uncertainties in the field distortions or registration, which will be taken into account by our use of an empirical point spread function. The resulting maps were co-added and processed to produce source lists in exactly the same fashion as the real data.

6.2 Results

Having extracted the sources from the simulated maps we can immediately use these to check for any biases or non-linearities in our flux estimation either from the peculiarities in the data reduction process or from the properties of the sky itself. Biases from the sky might arise through confusion (where faint sources are blurred together and add flux to identified sources) or Eddington bias (sometimes called

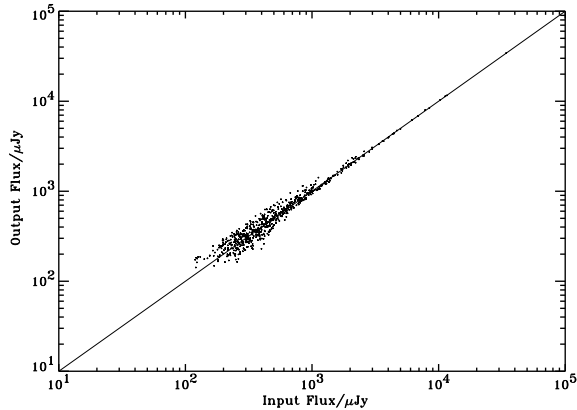


Figure 10. Output flux vs Input flux from the simulated data at $15\mu\text{m}$.

Malmquist bias, where even with a symmetric noise distribution, if the source counts are rising more sources are randomly scattered to brighter fluxes than are randomly scattered to faint fluxes). The first step is to associate the detected sources with the corresponding input source. To do this we use a $4''$ search radius and require that the ratio of the output and input fluxes does not exceed ± 0.3 dex.

The resulting comparisons are shown in Figures 9 & 10. At $6.7\mu\text{m}$ the results are highly linear and there appears to be no significant bias, while at $15\mu\text{m}$, where we expect the confusion noise to be higher, there is some evidence for a small tendency to over-estimate faint fluxes. For the purposes of this paper we ignore these small flux biases.

7 CATALOGUES

The simulations of Section 6 were used to investigate how to construct a highly reliable source list that could be described simply in terms of the quantities introduced in Section 4. We eventually decided on the following criteria:

- (i) $SNR0 > 3$: the initial candidate selection from the co-added maps
- (ii) all candidates located within a $2.5'$ radius of 22 32 56.2 -60 33 2.7 (J2000): this excludes regions of low $NPOINT$, non-Gaussian and/or higher noise, giving a clean and simple selection criterion
- (iii) $SNR5 > 1$: this excluded spurious sources generated from a strong noise feature in one map.
- (iv) for LW2 only, $PICK > 3$.

These criteria resulted in 24 sources being detected in the LW2 maps and an equal number being detected in the LW3 maps: from the simulations we estimate that the resulting source lists have 2.3 and 2.4 spurious sources, respectively, implying a reliability of about 90 per cent. The “completeness” of these

lists, expressed as an effective survey area, is discussed in Section 8.

For ease of comparison of our results with those from any possible future reductions of these data by other methods, we present our source catalogues with fluxes given in both instrumental and physical units, thereby decoupling issues of source detection, reliability and completeness from that of photometric calibration. In Tables 6 and 7 we list the separate source catalogues for the two bands, while Table 8 presents the results of merging these two catalogues. This was done through associating sources from different bands separated by less than 5 arcsec, which produced thirteen matches. The 5 arcsec radius was chosen to be slightly less than the Airy radius at $15\ \mu\text{m}$ (6 arcsec), larger than the astrometric errors which are discussed further in Paper II, yet small enough that there is little danger of association with an unrelated neighbouring source (the number of unrelated sources expected in a circle this size is 0.03, assuming a Poisson distribution). For those sources where no such match was found, we returned to the smoothed signal-to-noise map and if we found a signal-to-noise ratio above two we use the peak flux at this position (the assumption being that the rejection criteria which were applied to ensure reliability are not necessary since we have a confirmed detection in the other wavelength). Otherwise we determine an upper-limit, being the flux that would have given the observed smoothed signal if the noise fluctuation was -2σ . The absolute reference frame of the *ISO* data was set by making the position of the brightest $15\ \mu\text{m}$ source, ISOHDFS J223306-603350, coincident with that of the bright radio source HDFS J223306.0-603350 (A. Hopkins, *priv. comm.*) with which it is clearly associated, and then optimising the match between the *ISO* and optical positions of several of the bright stellar identifications of Paper II: this latter procedure only shifted the astrometric frames of the 6.7 and $15\ \mu\text{m}$ data by ~ 1 arcsec each.

The resulting $S_{6.7}/S_{15}$ colour-flux diagram is shown in Figure 11. Notice a reasonably clear distinction between stars and galaxies. For $\log_{10}(S_{6.7}/S_{15}) > 0.1$ all sources with an identification are morphologically classified as stars and occupy, or are consistent with, a well defined stellar locus with $\log_{10}(S_{6.7}/S_{15}) \sim 0.7$. Below $\log_{10}(S_{6.7}/S_{15}) < -0.3$ everything is morphologically non-stellar. In between these two limits are a mixture of sources. Firstly there are three stars which have upper limits at $15\ \mu\text{m}$ within this part of the diagram but are consistent with the colours of the other stars. Secondly there is one source (ISOHDFS J223243-603351) which has a broad line in its optical spectrum, and we thus assume that the relatively warm *ISO* colours are because the infrared emission arises from a dusty torus being heated by an AGN. This region and above also contains two of the three objects which had no reliable optical association (ISOHDFS J223256-603059 and ISOHDFS J223302-603137) as discussed

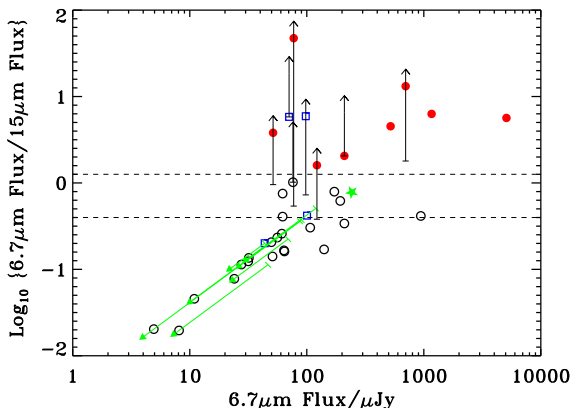


Figure 11. $6.7\ \mu\text{m}/15\ \mu\text{m}$ colour as a function of $6.7\ \mu\text{m}$ flux. Sources morphologically classified as stars are indicated with filled symbols, while other sources have open symbols. ISOHDFS J223243-603351, which has a broad line in the optical spectrum is indicated by 5-pointed star. Objects with no reliable optical counterpart are indicated by squares. Upper-limits are indicated by arrows, the tail of the arrow begins at the position given by the upper-limit, if a positive flux measurement was recorded the plotting symbol is placed at the position inferred from this measurement, otherwise the plotting symbol is placed at the tail of the arrow, which is then of arbitrary length. Upward-pointing arrows indicate upper-limits in the $15\ \mu\text{m}$ flux, arrows pointing to the bottom left indicate upper-limits in the $6.7\ \mu\text{m}$ flux.

in Paper II, and a third (ISOHDFS J223314-603203) which is one of the most uncertain identifications made there: in that paper we note that each of these is located close to a bright star which may mean that the sources are spurious, and will certainly affect their *ISO* colours. Of the four galaxies located firmly within this region we show in Paper II that three have SEDs consistent with normal spiral or cirrus galaxies (ISOHDFS J223243-603441, ISOHDFS J223302-603323 and ISOHDFS J223303-603336, the last of these has only an upper-limit at $15\ \mu\text{m}$) while the fourth ISOHDFS J223243-603242 does appear to have anomalously low $15\ \mu\text{m}$ flux indicating perhaps a deeper rest-frame $10\ \mu\text{m}$ absorption. Finally, two galaxies lie on the lower colour limit, one of these (ISOHDFS J223306-603349) is a bright spiral galaxy with a normal-spiral SED, while the second ISOHDFS J223254-603115 is associated with one of a pair of possibly interacting galaxies: this confuses the optical magnitudes is also likely to confuse the *ISO* colours. We also note that ISOHDFS J223256-603513, for which we are unable to make a secure optical identification, was the only source for which we recorded a negative $7\ \mu\text{m}$ flux measurement when determining the upper-limits.

In conclusion, it appears that the $7/15\ \mu\text{m}$ flux ratio separates quite neatly stars from star-forming

Table 6. Sources selected at $7\mu\text{m}$. SNR is estimated from the smoothed, co-added map. Flux (S , in instrumental units) is estimated from the peak in the smoothed map, the error is estimated from the standard deviation of the peak flux from independent rasters. $SNR5$ is S/σ . $PICK$ is the number of independent $SNRn > 1$ detections.

Name	RA & Dec (J2000)	SNR	S	σ	$SNR5$	$PICK$
ISOHDFSC7 J223315-603224	22 33 15.75 -60 32 24.0	205.8	5083.7	492.8	10.0	4
ISOHDFSC7 J223259-603118	22 32 59.50 -60 31 18.9	66.6	1165.9	74.6	15.8	4
ISOHDFSC7 J223306-603349	22 33 06.08 -60 33 49.1	62.2	943.0	8.3	113.9	4
ISOHDFSC7 J223303-603230	22 33 03.04 -60 32 30.6	38.8	520.2	69.1	7.6	4
ISOHDFSC7 J223237-603256	22 32 37.50 -60 32 56.7	32.3	699.4	79.4	8.6	4
ISOHDFSC7 J223243-603351	22 32 43.63 -60 33 51.0	15.1	242.5	30.2	8.1	4
ISOHDFSC7 J223250-603359	22 32 50.58 -60 33 59.9	14.9	209.4	31.4	6.7	4
ISOHDFSC7 J223243-603242	22 32 43.03 -60 32 42.2	10.6	171.9	39.9	4.1	4
ISOHDFSC7 J223312-603350	22 33 12.36 -60 33 50.7	10.6	209.4	68.4	3.2	4
ISOHDFSC7 J223243-603441	22 32 43.57 -60 34 41.6	9.1	193.2	42.0	4.6	4
ISOHDFSC7 J223245-603418	22 32 45.53 -60 34 18.0	8.3	140.6	56.7	2.5	4
ISOHDFSC7 J223308-603317	22 33 08.13 -60 33 17.8	6.8	107.0	25.6	4.0	4
ISOHDFSC7 J223237-603235	22 32 37.99 -60 32 35.5	5.9	122.1	46.3	2.4	4
ISOHDFSC7 J223303-603336	22 33 03.43 -60 33 36.0	5.5	76.2	14.1	5.1	4
ISOHDFSC7 J223302-603213	22 33 02.62 -60 32 13.3	5.3	77.3	37.6	2.2	4
ISOHDFSC7 J223256-603059	22 32 56.79 -60 30 59.2	4.9	98.0	35.2	2.7	4
ISOHDFSC7 J223247-603336	22 32 47.81 -60 33 36.6	4.5	63.8	41.0	1.6	4
ISOHDFSC7 J223302-603323	22 33 02.76 -60 33 23.5	4.5	62.2	12.5	4.9	4
ISOHDFSC7 J223253-603328	22 32 53.07 -60 33 28.1	4.3	56.0	20.1	2.7	3
ISOHDFSC7 J223254-603115	22 32 54.95 -60 31 15.1	3.4	62.2	28.4	2.3	3
ISOHDFSC7 J223254-603127	22 32 54.55 -60 31 27.8	3.0	51.0	19.3	2.5	3
ISOHDFSC7 J223302-603137	22 33 02.12 -60 31 37.5	4.3	70.6	46.2	1.4	3
ISOHDFSC7 J223307-603247	22 33 07.53 -60 32 47.0	4.1	64.4	30.0	2.0	3
ISOHDFSC7 J223254-603143	22 32 54.92 -60 31 43.8	3.5	51.5	23.2	1.8	3

Table 7. Sources selected at $15\mu\text{m}$. SNR is estimated from the smoothed, co-added map. Flux (S , in instrumental units) is estimated from the peak in the smoothed map, the error is estimated from the standard deviation of the peak flux from independent rasters. $SNR5$ is S/σ . $PICK$ is the number of independent $SNRn > 1$ detections.

Name	RA & Dec (J2000)	SNR	S	σ	$SNR5$	$PICK$
ISOHDFSC15 J223306-603350	22 33 06.08 -60 33 50.0	50.8	2274.2	15.8	142.1	4
ISOHDFSC15 J223245-603418	22 32 45.72 -60 34 18.3	15.4	826.5	70.8	11.7	4
ISOHDFSC15 J223315-603223	22 33 15.81 -60 32 23.6	12.4	899.9	248.4	3.3	4
ISOHDFSC15 J223312-603349	22 33 12.25 -60 33 49.6	10.5	617.1	67.6	8.6	4
ISOHDFSC15 J223247-603335	22 32 47.63 -60 33 35.5	8.7	385.1	156.1	2.3	4
ISOHDFSC15 J223307-603248	22 33 07.54 -60 32 48.8	8.6	399.6	66.8	5.2	4
ISOHDFSC15 J223245-603226	22 32 45.81 -60 32 26.1	8.4	412.7	56.7	6.7	4
ISOHDFSC15 J223257-603305	22 32 57.42 -60 33 05.7	8.1	308.8	118.0	2.4	4
ISOHDFSC15 J223308-603314	22 33 08.01 -60 33 14.9	7.6	352.1	96.4	3.5	4
ISOHDFSC15 J223254-603129	22 32 54.49 -60 31 29.7	7.1	361.6	96.5	3.3	4
ISOHDFSC15 J223251-603335	22 32 51.81 -60 33 35.1	6.2	255.2	56.1	4.2	4
ISOHDFSC15 J223252-603327	22 32 52.87 -60 33 27.9	6.1	239.8	58.2	3.7	4
ISOHDFSC15 J223243-603351	22 32 43.42 -60 33 51.6	5.9	310.9	4.4	70.6	3
ISOHDFSC15 J223243-603440	22 32 43.44 -60 34 40.7	4.7	312.0	158.9	2.0	4
ISOHDFSC15 J223306-603436	22 33 06.05 -60 34 36.6	4.3	241.6	95.6	2.8	3
ISOHDFSC15 J223306-603450	22 33 06.99 -60 34 50.8	4.2	242.4	64.0	3.8	3
ISOHDFSC15 J223243-603243	22 32 43.12 -60 32 43.3	4.1	216.9	88.6	2.5	3
ISOHDFSC15 J223312-603416	22 33 12.25 -60 34 16.9	3.7	236.6	72.2	3.1	3
ISOHDFSC15 J223244-603455	22 32 44.22 -60 34 55.3	3.5	239.5	99.0	2.6	3
ISOHDFSC15 J223256-603513	22 32 56.46 -60 35 13.2	3.4	217.8	31.8	6.8	3
ISOHDFSC15 J223259-603116	22 32 59.90 -60 31 16.6	3.3	185.3	48.6	3.6	4
ISOHDFSC15 J223244-603110	22 32 44.70 -60 31 10.0	3.1	242.7	52.9	4.7	3
ISOHDFSC15 J223240-603141	22 32 40.53 -60 31 41.0	3.1	235.5	45.6	5.3	4
ISOHDFSC15 J223314-603203	22 33 14.40 -60 32 03.4	3.3	240.1	178.2	1.0	2

Table 8. Merged *ISO* HDF South source list. The $6.7\mu\text{m}$ and $15\mu\text{m}$ source have been cross-correlated using a $5''$ search radius, and fluxes for non-matches are determined from the maps. Upper-limits are also estimated from the maps and denoted by “ $< S_{\text{up}}$ ”, where $S_{\text{up}} = S_{\text{obs}} + 2\sigma$, and σ is estimated from the scatter between independent maps at the source position and S_{obs} is the recorded flux at the source position (which may be negative). Sources marked with an asterisk do not have optical identifications (see Paper II). In most cases they are located near another bright source and are very likely to be spurious: their number is consistent with our simulations, and these “sources” have not been used in our number count analysis.

Name	$S_{6.7}$ / μJy	$\sigma_{6.7}$ / μJy	S_{15} / μJy	σ_{15} / μJy
ISOHDFS J223237-603256	699.4	79.4	< 389.9	168.4
ISOHDFS J223237-603235	122.1	46.3	< 321.1	122.5
ISOHDFS J223240-603141	< 119.4	43.7	235.5	45.6
ISOHDFS J223243-603242	171.9	39.9	216.9	88.6
ISOHDFS J223243-603441	193.2	42.0	312.0	158.9
ISOHDFS J223243-603351	242.5	30.2	310.9	4.4
ISOHDFS J223244-603455	< 53.6	21.3	239.5	99.0
ISOHDFS J223244-603110	< 90.4	31.4	242.7	52.9
ISOHDFS J223245-603418	140.6	56.7	826.5	70.8
ISOHDFS J223245-603226	< 46.7	19.3	412.7	56.7
ISOHDFS J223247-603335	63.8	41.0	385.1	156.1
ISOHDFS J223250-603359	209.4	31.4	< 101.9	66.5
ISOHDFS J223251-603335	31.6	28.9	255.2	56.1
ISOHDFS J223252-603327	56.0	20.1	239.8	58.2
ISOHDFS J223254-603129	51.0	19.3	361.6	96.5
ISOHDFS J223254-603143	51.5	23.2	< 53.9	20.2
ISOHDFS J223254-603115	62.2	28.4	152.5	57.2
ISOHDFS J223256-603513*	< 43.7	30.1	217.8	31.8
ISOHDFS J223256-603059*	98.0	35.2	< 134.8	59.1
ISOHDFS J223257-603305	< 69.3	22.6	308.8	118.0
ISOHDFS J223259-603118	1165.9	74.6	185.3	48.6
ISOHDFS J223302-603137*	70.6	46.2	< 12.1	9.0
ISOHDFS J223302-603213	77.3	37.6	< 143.3	70.8
ISOHDFS J223302-603323	62.2	12.5	82.5	106.0
ISOHDFS J223303-603230	520.2	69.1	114.9	65.1
ISOHDFS J223303-603336	76.2	14.1	< 74.7	40.6
ISOHDFS J223306-603436	49.8	19.8	241.6	95.6
ISOHDFS J223306-603349	943.0	8.3	2274.2	15.8
ISOHDFS J223306-603450	< 87.4	41.3	242.4	64.0
ISOHDFS J223307-603248	64.4	30.0	399.6	66.8
ISOHDFS J223308-603314	107.0	25.6	352.1	96.4
ISOHDFS J223312-603416	61.2	65.0	236.6	72.2
ISOHDFS J223312-603350	209.4	68.4	617.1	67.6
ISOHDFS J223314-603203	100.5	82.8	240.1	178.2
ISOHDFS J223315-603224	5083.7	492.8	899.9	248.4

galaxies, with AGN and normal galaxies occupying a middle ground. The *ISO* colours appear consistent with our optical morphological classifications: for the purposes of this paper we will use the morphological classifications and for the number count analysis will exclude the unidentified sources.

8 SOURCE COUNTS

8.1 Calculation of effective area

From the simulated catalogues we can directly determine the “completeness”, which we define in terms of the effective area as a function of flux; the effective area of the catalogue, at a given flux, being the area

within which a source of that flux could have been detected. We can estimate this from the simulations by determining the fraction of sources of a given input flux which pass all our selection criteria, and the effective area is then this fraction of the area over which the input catalogues were prepared: in practice we examine only those input source which fell within a $2.5'$ radius of $22\ 32\ 56.2\ -60\ 33\ 2.7$ (J2000). If the output flux is an unbiased estimator of the input flux this estimate of the effective area is unbiased. Eddington bias and confusion noise do cause some bias, as discussed in Section 6, but these appear to be small and are only second order effects in the calculation of effective area so we ignore them here. The resulting effective areas are illustrated in Figures 12 & 13.

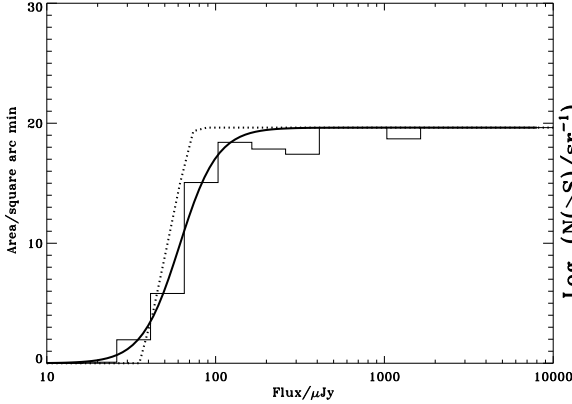


Figure 12. $6.7\mu\text{m}$ effective area as a function of flux. The histogram is estimated directly from fraction of sources detected from the simulated data as a function of input source flux. The dotted line is a naïve estimate based simply on the SNR selection criterion and the noise maps, while the solid line is a fit to the simulated histogram: $\Omega = 19.63\frac{1}{2} \tanh[4.47 \log_{10}(S/61.1\mu\text{Jy}) + 1]$ square arc min.

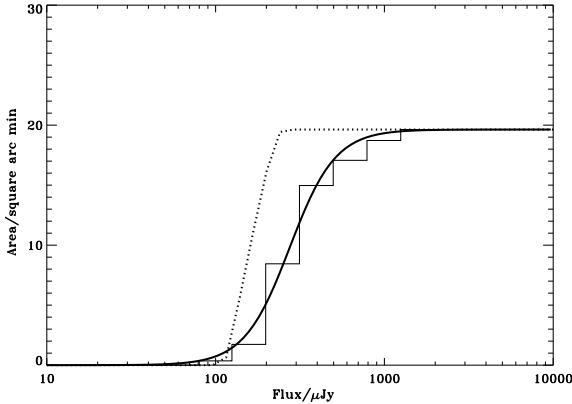


Figure 13. $15\mu\text{m}$ effective area as a function of flux. The histogram is estimated directly from fraction of sources detected from the simulated data as a function of input source flux. The dotted line is a naïve estimate based simply on the SNR selection criterion and the noise maps, while the solid line is a fit to the simulated histogram: $\Omega = 19.63\frac{1}{2} \tanh[3.70 \log_{10}(S/275\mu\text{Jy}) + 1]$ square arc min.

As with the ELAIS 6.7 and $15\mu\text{m}$ counts (Serjeant et al. 2000) we fit the histogram of the effective area with a hyperbolic tan function $\Omega = 19.63\frac{1}{2} \tanh[a \log_{10}(S/b) + 1]$ where a defines the gradient of the decline and b defines its location. For the $6.7\mu\text{m}$ simulations we find $a = 4.47$, $b = 61.1\mu\text{Jy}$ while for the $15\mu\text{m}$ simulations we find $a = 3.70$, $b = 275\mu\text{Jy}$. Also illustrated in Figures 12 & 13 are estimates of the effective area naïvely based on the noise maps used in constructing the SNR maps. Since this ignores some of the selection criteria it over-predicts

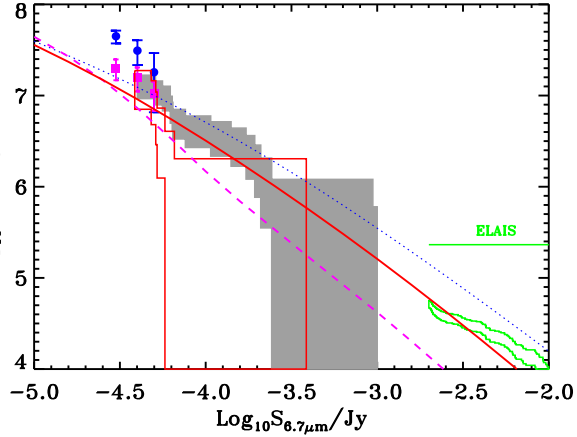


Figure 14. Extragalactic counts at $6.7\mu\text{m}$ from HDF South in this work (shaded region). Counts from other surveys are illustrated as follows: Abell 2390 (Altieri et al. 1999, filled circles); Lockman Hole (Taniguchi et al. 1997, filled squares); HDF North (Oliver et al. 1997, open region at faint fluxes); and ELAIS (Serjeant et al. 2000, open region). The models of Rowan-Robinson (2001) (solid); Pearson & Rowan-Robinson (1996) (dotted) and Franceschini et al. (1994) (short dashed) are plotted for comparison.

the fraction of sources detectable at brighter fluxes. On the other hand it takes no account of the boosting of faint input fluxes by confusion noise or Eddington bias and so under-predicts the effective area at faint fluxes. This illustrates that these simulations at least account for these biases to the first order.

8.2 Source Count Results

In Figures 14 and 15 we plot the resulting integral counts for galaxies (as defined by the colour criterion defined in Section 7). For comparison we also show the counts obtained by Oliver et al. (1997) for the HDF North. In Figure 15 we also show the counts derived by Aussel et al. (1999) from the same HDF North data.

At $6.7\mu\text{m}$ the galaxy counts from HDF North and South are in good agreement at the faint end, but the HDF South counts are higher at the brighter end. One possible explanation for this is that original selection of the HDF North field, which avoided bright galaxies, biased the bright counts downwards. Due to the observational strategies discussed in Section 2, the HDF South data at $6.7\mu\text{m}$ are considerably superior to the data from the North. The larger areal coverage in particular means the brighter counts are better constrained. So, while Oliver et al. (1997) suggested that the Pearson & Rowan-Robinson (1996) model could be ruled out, as it over-predicted the number of bright sources, we find that HDF South data are much more consistent with the Pearson & Rowan-Robinson model; indeed the Franceschini et al. (1994) model

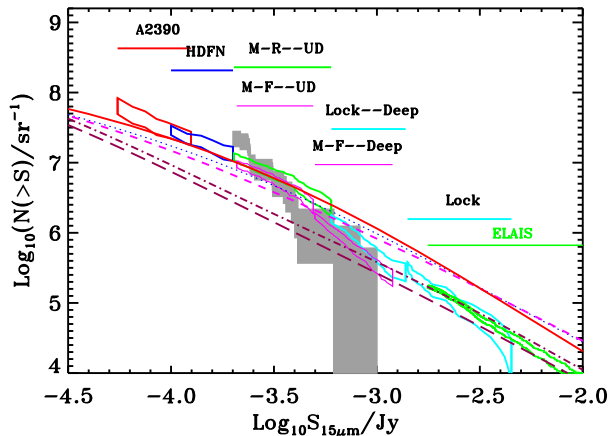


Figure 15. Extragalactic source counts at $15\mu\text{m}$ with the counts from HDF South in this work shown as a shaded region. Counts from other surveys are illustrated with open boxes and annotated above, in decreasing sensitivity: Abell 2390 (Altieri et al. 1999); Deep HDF North (Aussel et al. 1999); Marano-ROSAT Ultra-deep (Elbaz et al. 1999); Marano-Firback Ultra-deep (thin) (Elbaz et al. 1999); Marano-Firback Deep (thin) (Elbaz et al. 1999); Lockmann Deep (Elbaz et al. 1999); Lockmann Shallow (Elbaz et al. 1999); ELAIS (20). The models of Rowan-Robinson (2001) (solid); Pearson & Rowan-Robinson (1996) (dotted); Franceschini et al. (1994) (short dashed); Guiderdoni et al. (1998) model 'A' (long dashed); and Guiderdoni et al. (1998) model 'E' (dot-dash) are plotted for comparison.

now appears to be ruled out as it does not predict enough brighter $6.7\mu\text{m}$ sources. Such a conclusion is also borne out by the ELAIS counts (Serjeant et al. 2000) which are shown for comparison.

The $15\mu\text{m}$ HDF South data over the range $250 - 400\mu\text{Jy}$ are in striking agreement with Aussel et al. (1999) HDF North counts (which push the *ISO* data deeper than those of Oliver et al. 1997). If not coincidental, this agreement would suggest that these populations are at moderate-to-high redshifts. If all the sources had been located at low redshift the volume sampled within either HDF area (~ 20 square arcmin) would be small and the fluctuations due to cosmic variance large: e.g. if the sample were limited to $z < 0.5$, the fluctuations in this volume would be > 100 per cent (assuming a cubical geometry and the power spectrum of Peacock and Dodds 1994), while, even at $z < 1$ the fluctuations would be around 80 per cent (e.g. Oliver et al. 2000). Below $250\mu\text{Jy}$ the HDF South counts take a sharp up-turn. This flux level is also where the effective area drops, and where we are susceptible to errors in its calculation. We demonstrate in Paper II that the many of the sources appear to have modest redshifts and so the agreement between the HDF North and South brighter data may be coincidental, and the steep upturn could also be an effect of clustering. It would be possible to combine

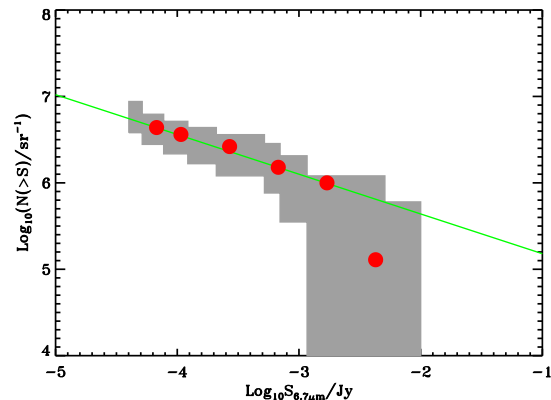


Figure 16. The star source counts at $6.7\mu\text{m}$ in the HDF South, shaded region. Circles indicate K-band star counts in the SGP transformed from (Minezaki et al. 1998) and the line indicates a fit to those data (excluding the brightest point)

the HDF North and South counts to produce a single determination of the counts over the $250 - 400\mu\text{Jy}$ regime, reducing the statistical errors by a factor of $\sqrt{2}$. Given the uncertainty in the effective area below $250\mu\text{m}$ both the Pearson & Rowan-Robinson (1996) model appear to provide acceptable fits to the counts. Both Guiderdoni et al. (1998) models appear to be too far below the counts.

The star counts at $6.7\mu\text{m}$ are shown in Figure 16. There are currently no published star count data at this wavelength and flux to compare these data with. However, it is possible to extrapolate from star counts at shorter wavelengths. Minezaki et al. (1998) present near infrared (K-band) star counts, towards the South Galactic Pole ($l = 316, b = -89$). Converting their differential counts into integral counts and using the K-band zero point of 673Jy we are able to compare their data with ours. With the exception of their brightest point, their data are fit with a power law $\log N(> S) = 4.72 - 0.46 \cdot S_K$. By coincidence, the same power law is consistent with our data. This is consistent with our detecting the same populations, since the slope is the same, but with a higher number density (as we would expect our stars to be fainter). Since we would expect to be in the Rayleigh-Jeans part of a Planck spectrum, we would expect our stars to be fainter by a factor of around 11, so the coincidence in normalization thus implies that the Hubble Deep Field South has about three times the number density of stars as the South Galactic Pole.

9 CONCLUSIONS

We have performed a survey using *ISO-CAM* at 6.7 and $15\mu\text{m}$ in the Hubble Deep Field South region. The observational and data reduction techniques that

we have employed mean that these data, and the $6.7\mu\text{m}$ data in particular, are significantly improved over the equivalent *ISO-HDF* data. From the resulting data we have extracted conservative bright source lists. We have thoroughly investigated the completeness and reliability of these lists using simulations. We have performed an external calibration of the data using stars in the field, a number of which have been spectroscopically classified. We find that the 6.7 and $15\mu\text{m}$ colour flux diagram provides a useful discriminant between stars and galaxies. We have investigated the number counts of the extra-galactic sources and stars. We find that the number counts of the extra-galactic sources are consistent with previous determinations, however, we stress that the volume sampled by our survey is likely to be small and so clustering effects (cosmic variance) may mean that this agreement is somewhat coincidental. A steep upturn at the faintest fluxes is due to only a few sources and is almost certain to be an effect of clustering. Further details of this project can be found at astro.ic.ac.uk/hdfs).

ACKNOWLEDGMENTS

We would like to thank the anonymous referee for rapid and constructive feedback. This paper is based on observations with *ISO*, an ESA project, with instruments funded by ESA Member States (especially the PI countries: France, Germany, the Netherlands and the United Kingdom) and with participation of ISAS and NASA. This work was in part supported by PPARC grant no. GR/K98728 and EC Network is FMRX-CT96-0068. We thank the ATNF HDF-S team, particularly Andrew Hopkins, for providing us with radio data for our sources in advance of publication.

REFERENCES

- Altieri, B. et al. 1999, *A&A*, 343, L65
 Aussel H., Cesarsky C.J., Elbaz D., Starck J.L., 1999, *A&A*, 342, 313
 Cesarsky C.J., et al., 1996, *A&A*, 315, L32
 Cram L., Hopkins A., Mobasher B., Rowan-Robinson M., 1998, *ApJ*, 507, 155
 da Costa L., et al., 1998, (astro-ph/9812105)
 Desert F.-X., Puget J.-L., Clements D.L., Perault M., Abergel A., Bernard J.-P., Cesarsky C.J., 1999, *A&A*, 342, 363
 Elbaz D., et al., 1999, *A&A*, 351, L37
 Flores, H., et al. 1999, *ApJ*, 517, 148
 Franceschini A., Mazzei P., De Zotti G., Giann F., Danese L., 1994, *ApJ*, 427, 140
 Gardner J.P., et al., 1999, <http://hires.gsfc.nasa.gov/~gardner/hdfs/>
 Glazebrook K., et al., 2002, in preparation
 Goldschmidt P., et al., 1997, *MNRAS*, 289, 465
 Guiderdoni B., Hivon E., Bouchet F.R., Maffei B., 1998, *MNRAS*, 295, 877
 Kessler M.F., 1996, *A&A*, 315, L27
 Mann R.G., et al., 1997, *MNRAS*, 289, 482
 Mann R.G., et al., 2002, *MNRAS*, submitted
 Minezaki, T., Yoshii, Y., Cohen, M., Kobayashi, Y. and Peterson, B. A. 1998, *AJ*, 115, 229
 Oliver S.J., et al., 1997, *MNRAS*, 289, 471
 Oliver S.J., et al., 2000, *MNRAS*, 316, 749
 Ott S., et al., 1998, in *Astronomical Data Analysis Software and Systems VII*, (eds.), R. Albrecht, R.N. Hook & H.A. Bushouse. A.S.P. Conference Series, Vol. 145, p. 275
 Peacock J.A., Dodds S.J., 1994, *MNRAS*, 267, 1020
 Pearson C., Rowan-Robinson, M., 1996, *MNRAS*, 283, 174
 Rowan-Robinson M., 2001, *ApJ*, 549, 745
 Rowan-Robinson M., et al., 1997, *MNRAS*, 289, 490
 Salpeter E.E., 1955, *ApJ*, 121, 161
 Serjeant S.B.G., et al., 1997, *MNRAS*, 289, 457
 Serjeant S.B.G., et al., 2000, *MNRAS*, 316, 768
 Steidel, C. C., Adelberger, K. L., Giavalisco, M., Dickinson, M. & Pettini, M. 1999, *ApJ*, 519, 1
 Taniguchi Y., et al., 1997, *A&A*, 328, L9
 Verma A., et al., 2002, in preparation
 Walker A., 1999, http://icarus.stsci.edu/~ferguson/hdfstest/hdfs_astro.fits
 Williams R.E., et al., 1996, *AJ*, 112, 1335